

# Investigation of Oxide Dispersion Strengthening Effect on the Strength of Diffusion-Bonded AISI304 Parts

Thomas Gietzelt,\* Mario Walter, Volker Toth, Florian Messerschmidt, and Melina Blem

In this article, experiments for reinforcing diffusion-bonded AISI304 parts by the oxide dispersion strengthening (ODS) effect (oxide dispersion strengthened) are performed. Small particles, insoluble with temperature, act as obstacles for the dislocation movement. Thin sheet material as a carrier for ceramic particles of different sizes (0.5 and 50  $\mu\text{m}$ , respectively) is used as an interlayer in diffusion bonding experiments. Furthermore, ceramic particles facilitate penetration of stable passivation layers, enabling atomic diffusion across bonding planes. However, a ceramic–metallic interface cannot transfer mechanical load. Hence, the strengthening effect must exceed the weakening of the cross-sectional area caused by the ceramic particles. It is found that an equal distribution of ceramic particles in the interlayer is challenging. Dip coating for 0.5  $\mu\text{m}$  alumina is more suited than a mechanical arrangement of beads several tens of micrometers in size in etched holes or calottes. Samples fail in the interface region due to imperfect inclusion of ceramic particles. It turns out that it is difficult to separate the impact of the smaller grain size of the thin sheet material compared to round stock (Hall–Petch relation) on the one hand from the reinforcing effect from the incorporation of ceramic particles.

low. Heating and cooling in vacuum are slow, leading to long batch time and causing high costs.

In diffusion bonding, parts to be joined are subjected to elevated temperatures. An external load is applied to level surface asperities and ensure intimate contact at microscopic scale.

All stages and the processes involved are discussed in detail in.<sup>[1]</sup> By diffusion processes of atoms, a sound joint is formed. It is accompanied by grain growth and grain boundary movement across the bonding plane. A monolithic part is formed, and the mechanical properties ideally correspond to those of the material, which has been subjected to an identical heat treatment. However, in literature, often data are published, where only a certain percentage of a mechanical parameter (yield and tensile strength, respectively, elongation at fracture)<sup>[2–5]</sup> is achieved. It must be assumed that decreased mechanical values

are due to imperfect diffusion bonding. Often, pores are found, or passivation layers prevent appropriate bonding. This should not be state of the art, especially for safety-relevant components such as pressure vessels in nuclear power plants.

For corrosion resistant materials, the chemical stability of the passivation layers depends also on the level of alloying elements forming these layers, e.g., chromium, silicon, and aluminum. Depending on their chemical stability, thickness, and defects contained, it must be removed or at least partially penetrated to enable atomic diffusion. Otherwise, it decreases or hinders diffusion of atoms across bonding planes. For this, the deformation of surface asperities or the presence of hard particles in the bonding plane are helpful.

Sometimes, it might be impossible to achieve perfect bonding all over the device, e.g., in multilayered assemblies, where for design reasons different effective bonding areas per bonding layer apply, leading to varying contact pressure in individual layers.<sup>[6]</sup>

The mechanical strength is directly related to the grain size (*Hall–Petch relation*). Since grain growth accompanies diffusion bonding, the incorporation of small ceramic particles may help to suppress it by exploiting the ODS effect in the bonding plane. In consequence, locally, a higher strength could be achieved, compensating for the mechanical decay by remaining pores and grain growth.

A similar approach was described in,<sup>[7]</sup> where the formation of finely distributed carbides in the bonding zone and dynamic


## 1. Introduction

### 1.1. Diffusion Bonding, Arising Issues, and How Oxide Dispersion Strengthening (ODS) Could Contribute to Increasing the Mechanical Properties of the Bonding Plane

For energetical reasons and to prevent oxidation, diffusion bonding is carried out under high vacuum to minimize heat transfer to the recipient wall and to keep energy consumption

T. Gietzelt, M. Walter, V. Toth, F. Messerschmidt, M. Blem  
Institute of Micro Process Engineering  
Karlsruher Institut für Technologie (KIT)  
PoBox 3640, 76021 Karlsruhe, Germany  
E-mail: thomas.gietzelt@kit.edu

T. Gietzelt, M. Walter, V. Toth, F. Messerschmidt, M. Blem  
Institute for Applied Materials – Mechanics of Materials and Interfaces  
Karlsruher Institut für Technologie (KIT)  
76021 Karlsruhe, Germany

 The ORCID identification number(s) for the author(s) of this article can be found under <https://doi.org/10.1002/adem.202500616>.

© 2025 The Author(s). Advanced Engineering Materials published by Wiley-VCH GmbH. This is an open access article under the terms of the Creative Commons Attribution License, which permits use, distribution and reproduction in any medium, provided the original work is properly cited.

DOI: 10.1002/adem.202500616

recrystallization by deformation of surface asperities decreased grain growth. Good results, namely for elongation at fracture and impact toughness, were reported. For higher bonding temperatures, however, the particles were solved in the matrix for thermodynamic reasons.

## 1.2. Impacts Leading to Insufficient Diffusion Bonding and Degradation of Material Properties

### 1.2.1. Pores and Intermediate Layers

Several publications on diffusion bonding of a wide range of different materials state reduced mechanical properties in the bonding zone, most due to remaining pores, incompletely bonded interface, or the formation of brittle precipitations.<sup>[5,8–11]</sup> Pores can only be closed by volume diffusion, which is time controlled and several orders of magnitude lower than interfacial diffusion.<sup>[12,13]</sup> Hence, long dwell times are necessary. Instead, it is often recommended that design calculations should be based on a yield strength or elongation at fracture reduced by a certain percentage. From a material scientific point of view, such an approach is not satisfactory since it is not possible to guarantee a constant and reproducible mechanical strength under all circumstances. If the diffusion bonding process is controlled satisfactory, no defects remain in the bonding zone, and grain boundary migration across bonding planes occur.

Some reasons for the remaining pores and way out should be described:

Residual pores result from insufficient leveling of the surface asperities might be caused by insufficient contact pressure and/or too short dwell time. For temperature, the coefficient of diffusion changes exponentially. In the range of 1000 °C, a change in temperature of about 20 K results in doubling or halving of diffusion coefficient for stainless steel. If the temperature is set too low, pores can hardly be closed by volume diffusion. Both temperature and contact pressure exhibit opposite and nonlinear effects to the macroscopic deformation.<sup>[1,14]</sup> Furthermore, it is affected by the geometric dimensions of the parts to be joined.<sup>[15]</sup>

Hence, it is hard to specify constant and appropriate values for bonding temperature and contact pressure for arbitrary parts and to prevent excessive deformation at the same time.

Due to long dwell time at high temperature, brittle phases may be formed between different materials, according to phase diagrams, near the thermodynamic equilibrium. For complex alloys, precipitations or accumulation of impurities are formed at grain boundaries.

Employing intermediate layers, e.g., copper or nickel, may result in decreasing mechanical properties due to ductility and depending on thickness of the interlayer, solubility to bulk materials, and diffusion coefficient, depending on dwell time and bonding temperature. On the other hand, interlayers may prevent the formation of brittle intermetallic phases according to phase diagrams.<sup>[16–18]</sup>

The question arises on how mechanical properties of the diffusion bonding plane can be improved in such a way that failure always occurs in the base material.

### 1.2.2. Changes in Lattice Defects by Diffusion Bonding

The mechanical properties of a material are mainly defined by taking advantage of lattice defects of different dimensionality. Most are considerably subjected to decay during diffusion bonding.

The first impact arises from a drastically reduction of 1D lattice defects, e.g., dislocations: at high temperatures, due to the thermally activated mobility of atoms and its diffusion, dislocations start climbing and annihilation. In consequence, the dislocation density can be decreased by several orders of magnitude. Any cold work hardening effect of half stock is lost, which decreases the mechanical strength considerably.

A second impact is due to the change of 2D lattice defects, e.g., the grain size: diffusion bonding is accompanied by thermally activated grain growth. The driving force is the minimization of interfacial energy.<sup>[19–21]</sup> The interface per unit of volume is reduced, resulting in coarsening of the grain structure. In consequence, mechanical properties decrease according to *Hall–Petch relation* due to increased free path length of dislocation movement.<sup>[22,23]</sup> In the case of polymorphic materials, grain growth can be reversed by new formation of the grain structure twice, namely when heating above the transition temperature and when cooling down.<sup>[24]</sup>

Both effects, in addition to the constraints described below, must be taken into account, when considering diffusion bonding as a joining technique. In most cases, the mechanical strength of a material will be decreased by diffusion bonding.

Further constraints for hindering the formation of a sound joint by diffusion bonding are as follows:

A thin passivation layer may increase corrosion resistance by increasing chemical resistance. However, it hinders atomic diffusion and grain boundary movement across the bonding plane.

No grain boundary movement during diffusion bonding is also observed for ODS materials: the grain boundaries are pinned at nanoscaled obstacles, acting as 3D lattice defects, and the dislocation movement is suppressed. The reinforcing effect by 3D defects, incoherent to the base lattice, is maximum, if size and distribution are optimized to decrease the free path length of dislocation movement, especially at high temperatures.<sup>[25]</sup> On the other hand, incoherent interfaces are weakening the transfer of external forces in a diffusion-bonded interface, according to its percentage area, since no cohesion between both phases apply.<sup>[26]</sup>

For diffusion bonding, it means that higher mechanical strength can be achieved in the bonding plane by incorporation of small ceramic particles, whereas the strength of the bulk material decreases due to the decreased dislocation density and grain growth. In this way, it should be possible to compensate for small bonding defects in the bonding plane. By shifting the spot of failure to the bulk material, the bonding plane is not the weak point anymore.

A similar approach was reported by O. Cooke in.<sup>[27]</sup> The effect of a copper interlayer of several micrometers containing alumina nanoparticles was studied in terms of hindering the formation of intermetallic phases when diffusion bonding super-duplex-stainless steel to TiAl6V4. Whereas copper would be expected to show a very soft behavior after thermal treatment of diffusion bonding, alumina particles act for reinforcing.

Furthermore, the alumina particles caused a change in morphology of the intermetallic phases formed, depending on bonding temperature and dwell time.

In this article, diffusion bonding experiments, involving two sorts of ceramic particles different in size, were performed.

More problems arise for ferritic or especially for austenitic stabilized stainless steels according to the *Schaeffler* diagram and austenitic nickel base alloys: if the face-centered cubic lattice of an austenitic stainless steels is stabilized up to the melting temperature, the coefficient of diffusion is about two orders of magnitude lower than for the body-centered cubic lattice of ferritic steels.<sup>[28]</sup> In consequence, for face-centered cubic stainless steels, longer dwell time at higher temperatures is necessary to obtain a reasonable coefficient of diffusion and to close remaining pores. For this reason, neither appropriate diffusion bonding parameters nor the deformation behavior of ferritic and stainless steels can be compared.

### 1.2.3. Manufacturing of Material: Impact on Grain Size and Passivation Layer

For manufacturing of thin sheet material less than 3 mm in thickness, cold rolling is used to achieve tight tolerances in thickness.<sup>[29,30]</sup> By this, the dislocation density is increased by several orders of magnitude, accompanied by cold work hardening.<sup>[31]</sup> To decrease rolling force and limiting wear of the rolls, intermediate recrystallization heat treatments are performed between subsequent rolling steps.<sup>[32]</sup> By this, the dislocation density is reduced, and a fine-grained microstructure is obtained. Therefore, the grain size of thin sheet material is often about one order of magnitude smaller than for plate material several millimeters in thickness, and the strength is higher.<sup>[33]</sup> Recrystallization during the diffusion bonding process facilitated the formation of a sound bond.<sup>[34]</sup>

On the other hand, recrystallization heat treatment during manufacturing processes for half stock may reinforce the passivation layer of stainless steels to several hundred nanometers.<sup>[35,36]</sup> This is one reason for varying results of diffusion bonding of materials possessing passivation layers, which are insoluble in the matrix material and hinders diffusion of atoms.

### 1.2.4. Relationship Between Surface Roughness and Residual Pores

It is widely reported that surface asperities and its patterns and deformation during application of contact pressure in diffusion bonding play a major role for extending areas of microscopic

contact at atomic scale.<sup>[37–43]</sup> This deformation depends on the level of temperature as well as on contact pressure. Both parameters have opposite effects. The deformation of surface asperities is superimposed in competition with the macroscopic deformation by plastic flow of the material. Therefore, the contact pressure cannot be increased arbitrarily. Depending on the machining process of surfaces, different roughness patterns with different density of peaks and grooves are produced (**Figure 1**). It is clear that the given bonding temperature and contact pressure result in different percentage fractions of atomic surface contact areas. The remaining pores in between weaken the bond and must be filled by volume diffusion during dwell time, to ensure good mechanical properties as well as high vacuum tightness.<sup>[14]</sup>

On the other hand, surface asperities may be helpful to penetrate passivation layers. The same effect can be achieved by hard particles of appropriate size in the bonding plane. Inside grains, precipitates may be formed by an appropriate heat treatment of an alloy possessing a limited solubility of foreign atoms in the matrix. Individual steps are solution annealing, quenching, and subsequent aging. In contradiction to small ceramic particles, such precipitates are not stable at high temperatures.<sup>[44,45]</sup> For ceramic particles, however, there is no interaction with the metallic lattice. A ceramic–metallic interface can transfer external load only by micromechanical interlocking. Therefore, the ODS effect must exceed the deterioration in strength due to an increase in strength caused by the inhibition of dislocation movement. The challenge is to achieve the right size and distribution of small ceramic particles in the bonding plane.<sup>[46]</sup>

## 2. Materials and Diffusion Bonding Experiments

### 2.1. Materials and Design of Experiments

As material, round stock 40 mm in diameter, made of austenitic stainless steel 1.4301 (AISI 304), was used. Cylinders 40 mm in height at a tolerance of  $\pm 0.05$  mm were turned on a lathe.

For diffusion bonding experiments, two cylinders were stacked, giving an aspect ratio of two.

In between, different setups were arranged containing ceramic particles to study the reinforcing effect. First, a thin sheet made of AISI 304, 50 mm in diameter and a thickness of 0.2 mm, containing etched calottes with a nominal diameter of 55  $\mu\text{m}$  at a center-to-center distance of 255  $\mu\text{m}$  within a diameter of 25 mm, was placed (**Figure 2**). Second, microsieves made of AISI 304 by chemical etching, 50  $\mu\text{m}$  in thickness and

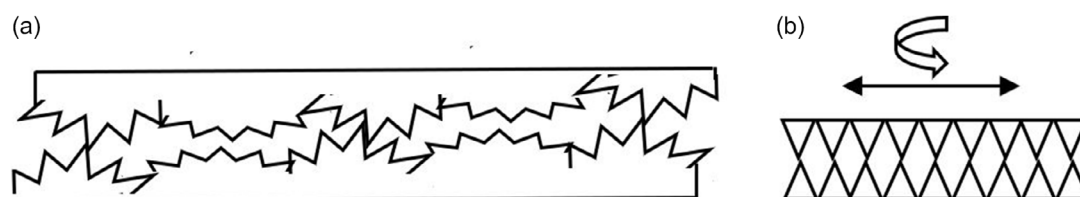


**Figure 1.** Schematic illustration of different surface roughness profiles leading to variation of the deformation of surface asperities and remaining pores. a) Irregular roughness profile, e.g., from lapping or polishing. b) Periodic roughness structure, e.g., from turning or milling. Different orientations of mating surfaces may apply.

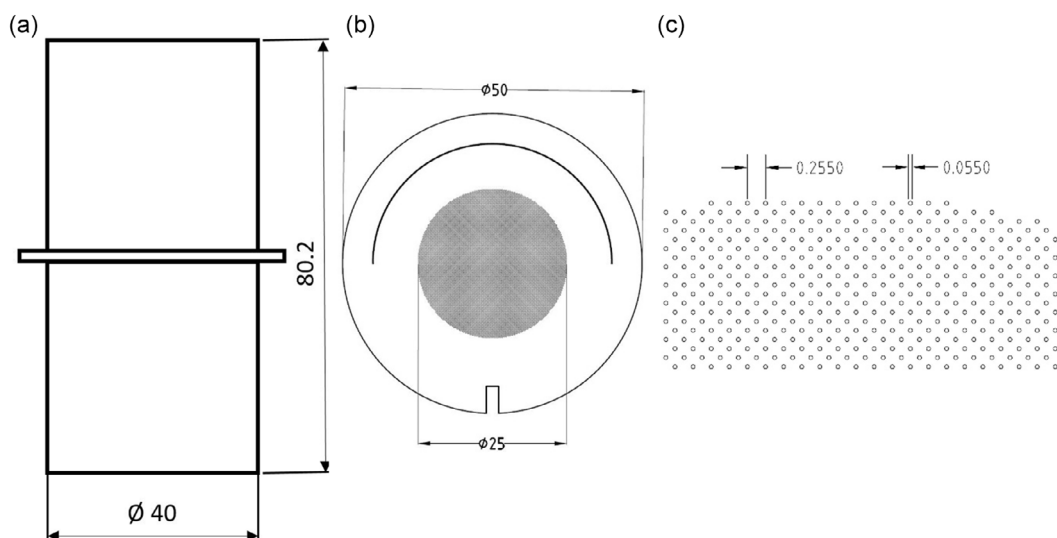


**Figure 2.** a) Diffusion bonding samples,  $d = 40$ ,  $h = 80.2$  mm. b) Design of etched sheet 0.2 mm in thickness with microcalottes within  $d = 25$  mm to immobilize zirconia beads. c) CAD-pattern of etched calottes. Numbers indicate hole diameter and center-to-center-distance in millimeter.

containing holes ranging from 60 to 80  $\mu\text{m}$  for zirconia beads 30 and 50  $\mu\text{m}$  in diameter, respectively, were evaluated. It must be noticed that thicker sheet material containing calottes was favorable for handling. For diffusion bonding experiments, a calotte sheet containing zirconia beads with a diameter of 50  $\mu\text{m}$  was preferred. Zirconia beads were supplied by *Tosoh Corporation*, Tokyo, Japan.<sup>[47]</sup>

Third, several 100  $\mu\text{m}$  layers of AISI304, coated with submicron alumina particles, were used. Details are given in subsequent sections.

## 2.2. Etching of Calottes

The CAD design of the thin sheet containing calottes (Figure 2b) was supplied by *Tecan*, Weymouth, UK, as well as by *Ätztechnik Herz GmbH*, Epfendorf am Neckar,

Germany. A photomask with a guiding structure for alignment with respect to the cylindrical diffusion bond samples and a recess for removing excessive zirconia beads (Figure 2b, at the bottom) was made and etched into sheets made of 1.4301 (AISI 304), 0.2 mm in thickness.

For the etched calottes, certain variations in the diameter were observed, depending on supplier and material. The etched calottes supplied by *Tecan* in 1.4301 were found to be flat and far away from being semicircular (Figure 3). It was concluded that it would be useless trying to fill it with zirconia beads.

By *Herz Ätztechnik*, etched calottes for two materials, namely 1.4301 and 1.4828Mo, were supplied. According to the delivery state F1700-1900 for 1.4028Mo, the material was in hardened condition. Surprisingly, calottes etched in 1.4028Mo showed a more uniform and semicircular pattern than for 1.4301 (Figure 4).

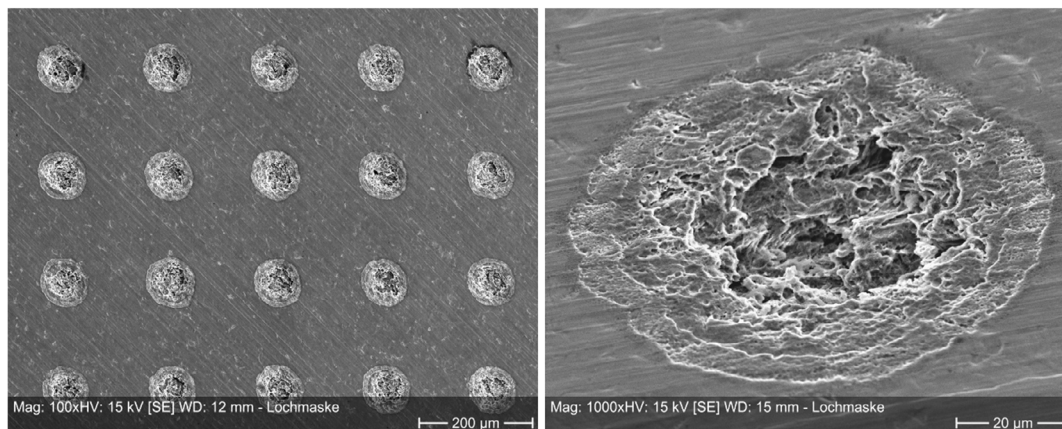


**Figure 3.** SEM details of calottes etched in 1.4301 (X5CrNi18-10, AISI 304) by Tecan.



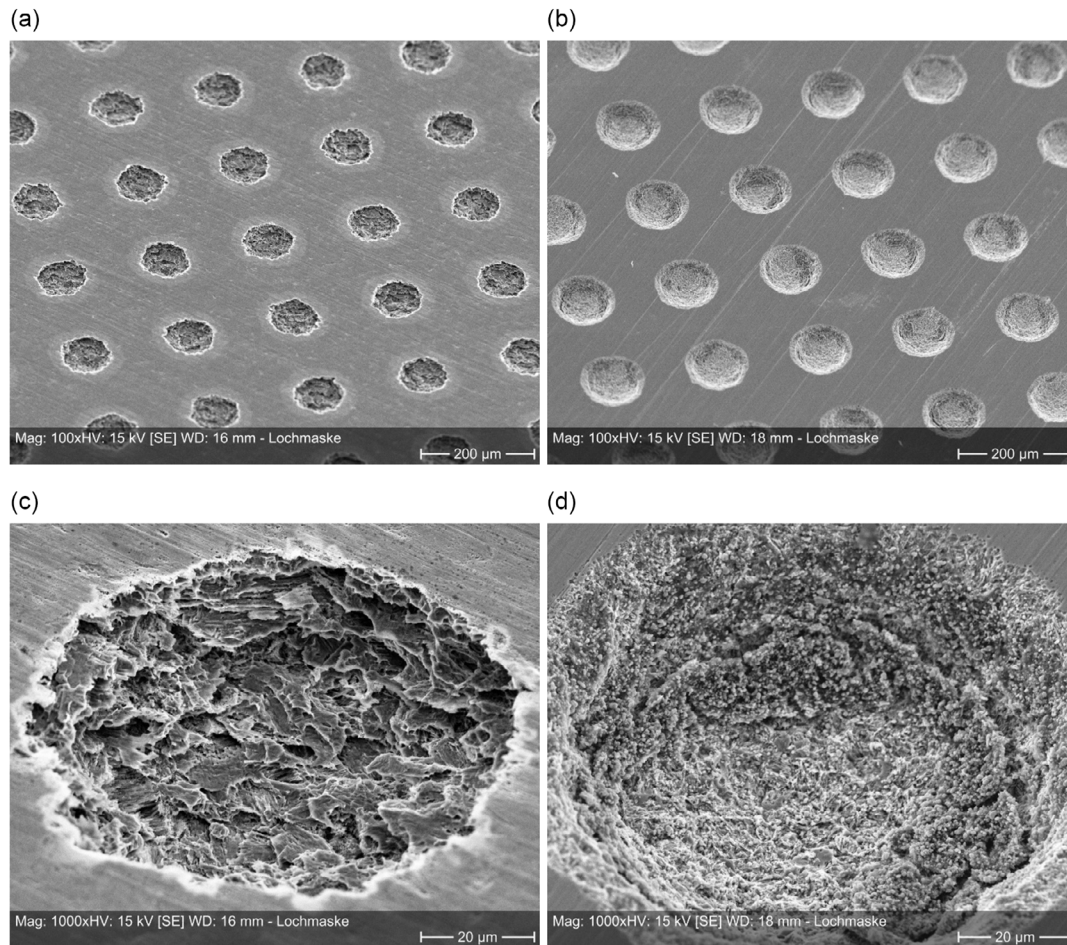


**Figure 4.** SEM details of calottes etched by Ätztechnik Herz. a,c) Etched in 1.4301 (X5CrNi18-10, AISI304). b,d) Etched in 1.4028Mo (X30Cr13, AISI 420B).

### 2.3. Etching of Microsieves

Microsieves were etched by Herz Ätztechnik in austenitic stainless steel AISI304 (1.4301) to evaluate the simplification and improving the immobilization of zirconia beads inside holes. The assumption was that it is easier to place the beads inside holes if the diameter of beads and the sheet thickness are close. Additionally, it prevents filling of multiple beads per hole. The zirconia beads can be forced across the surface, filling all holes. Excessive beads can be stripped off by a squeegee afterwards.

For manufacturing of microsieves, double-side etching was employed. The thickness of the sheet material was 0.05 mm. Since the limitation of etch depth is  $\approx 80\%$  of the diameter, holes 60 μm in diameter can be etched. However, certain lateral tolerances of positioning the photomasks on both sides applies.

To evaluate the quality and reproducibility of etching of small holes, variations of design were developed. Two hole diameters, namely 60 and 80 μm, respectively, were chosen, in combination with three different hole center distances of 255, 350, and 450 μm, respectively (Figure 5).

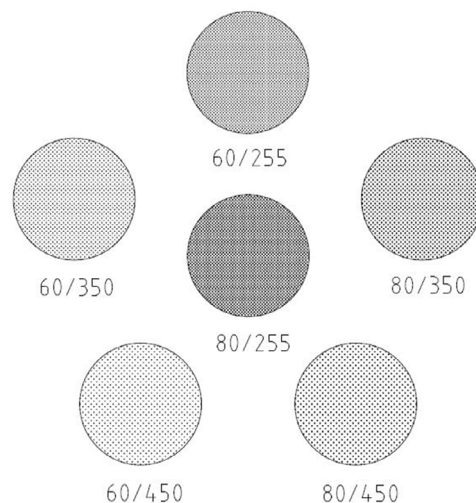


**Figure 5.** Different designs of holes and center-to-center distances for double-sided etching of microsieves. The first number indicates the hole diameter, and the second number the center-to-center distance. Distances are given in micrometers.

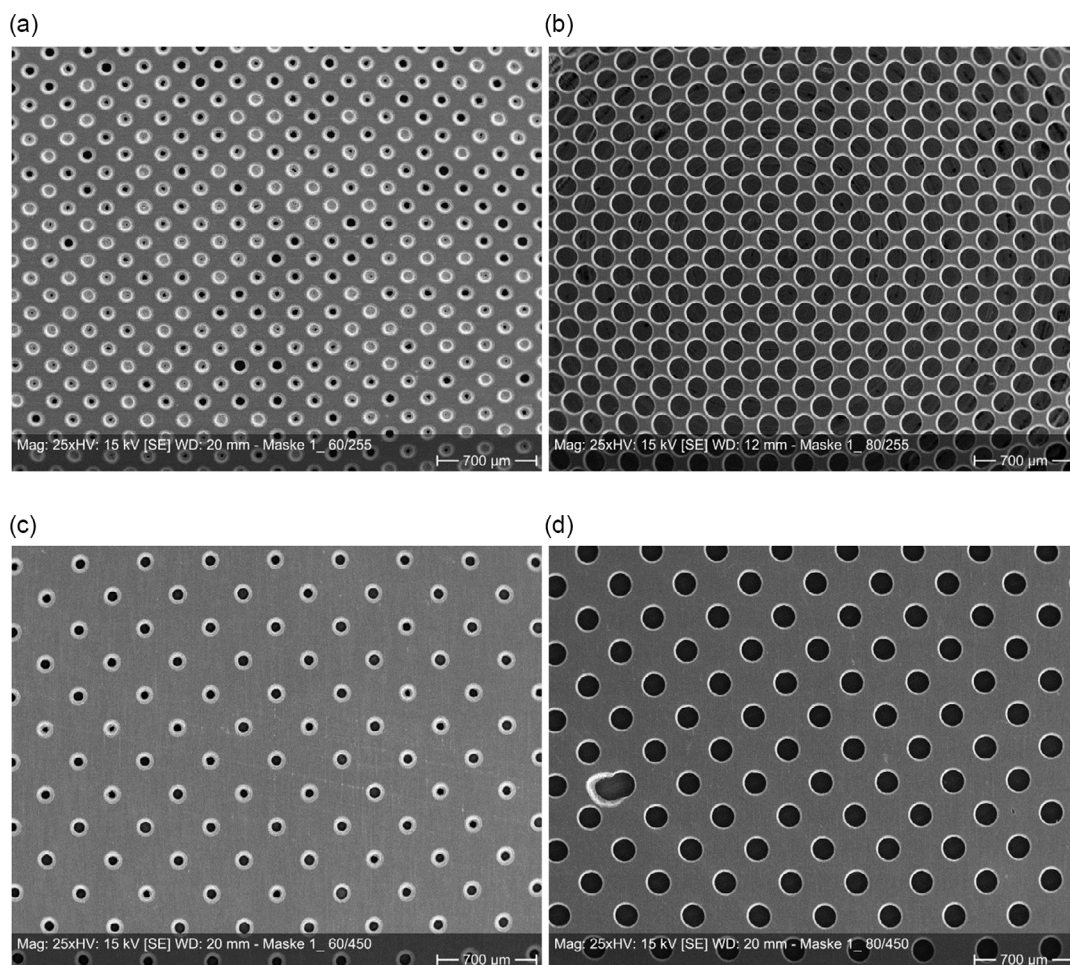


**Figure 6.** Etch results of designs depicted in Figure 5. a,b) For 60  $\mu\text{m}$  holes. Right: for 80  $\mu\text{m}$  holes. Top: for a hole center distance of 255  $\mu\text{m}$ . c,d) Hole center distance of 450  $\mu\text{m}$ , respectively.

Scanning electron microscopy (SEM) pictures were taken on different etches sheets. An example is given in **Figure 6**. It showed that the results varied from sheet to sheet and from design to design. Not all the 60  $\mu\text{m}$  holes are through-etched for a center-to-center distance of 255  $\mu\text{m}$ ; however, they are for a center-to-center distance of 450  $\mu\text{m}$ .

At a more detailed view, it was recognized that not only the reproducibility of etching varied but also the diameter of holes according to double-sided etching varied by the formation of etch burr at the contact plane (**Figure 7**).

## 2.4. Manipulation and Immobilization of Zirconia Beads

### 2.4.1. Immobilization of Zirconia Beads in Etched Calottes

Diffusion bonding experiments containing ceramic beads in the bonding plane were planned, using two sizes of zirconia beads, 30 and 50  $\mu\text{m}$ , respectively (**Figure 8**).

Unfortunately, it turned out that it was very challenging to put the zirconia beads in place on the etched calottes. It was not possible to roll the beads over the surface, so an increasing number

of beads hit the calottes and were immobilized there, as known from a game of patience. Due to the small size, attractive forces led to agglomeration. For 30  $\mu\text{m}$  zirconia beads, mostly two to four beads were trapped into one calotte; however, there were also spots where much more beads agglomerated around the calottes (top of **Figure 9**).

For the 50  $\mu\text{m}$  zirconia beads, more calottes could be filled with just one bead; however, there were a reasonable number of calottes left without zirconia beads. The agglomeration was not as strong as observed for the 30  $\mu\text{m}$  beads, but there were also spots with concentrations of beads (**Figure 9b,e**).

### 2.4.2. Immobilization of Zirconia Beads in Etched Microsieves

Based on the experience with the immobilization of zirconia beads in calottes, it was assumed that utilization of etched microsieves would be favorable if the sheet thickness is close to the diameter of the beads. Selected double-etched sheets were placed on a 40 mm round stock and fixed by four laser welding spots. The zirconia beads could be forced across the surface, filling all



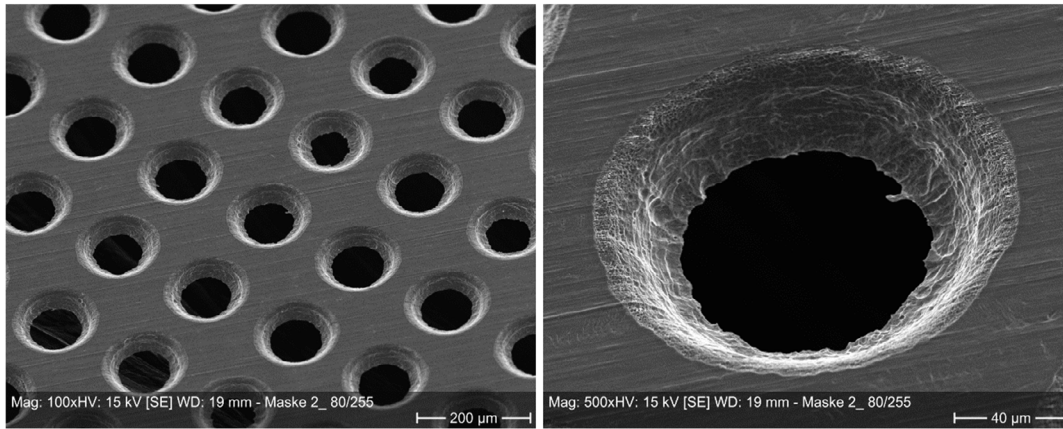


Figure 7. Etch burr from double-sided etching of holes.

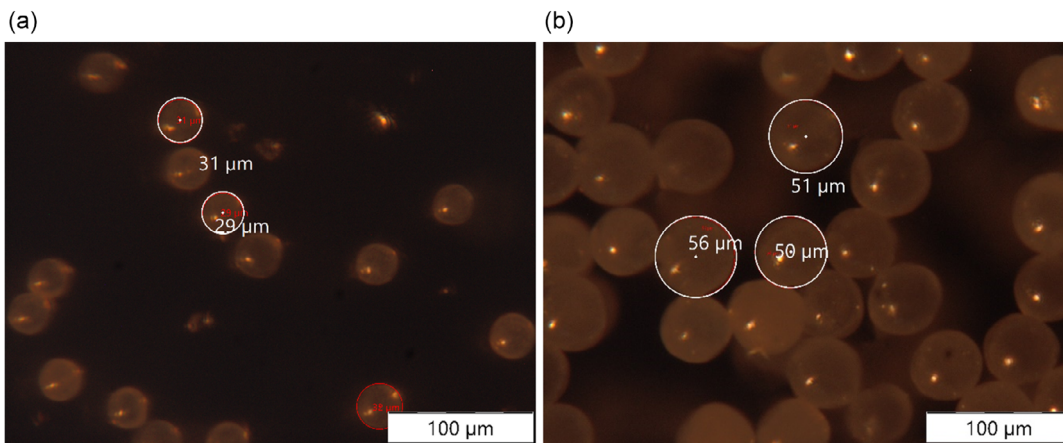


Figure 8. Light microscopic images of zirconia beads. a) 30 µm in diameter. b) 50 µm in diameter.

recesses and excessive beads can be stripped off by a squeegee after filling. However, due to a small gap between the micro-sieves and the round stock, additional beads got in between both layers, so no reproducible results could be achieved in the arrangement. This new effect cannot happen in case of sheets with etched calottes only. Hence, it was decided not to follow this approach, especially after the first diffusion bonding experiment using a calotte sheet was obtained, displaying no reinforcing effect for zirconia beads.

### 2.5. Dip Coating of 100 µm Stainless Steel Sheets (AISI304) with Submicron-Sized Alumina

For coating of stainless steel sheets 100 µm in thickness, 150 mL of an aqueous solution containing 2% of a sodium carboxymethyl cellulose polymer TEXTURECEL 2000 PA 07<sup>[48]</sup> together with 0.34 g of alumina Baikowski CR6 with a  $d_{50} = 0.5 \mu\text{m}$ <sup>[49]</sup> was prepared by stirring in an ultrasonic bath for  $t = 5$  min. After turning off the ultrasound, sheets were slowly immersed, retracted, and dried under ambient condition. Adhering alumina particles and its distribution can be seen in Figure 10. Although there were

some spots of accumulation, the distribution was rather uniform and at much smaller scale of size than for zirconia beads.

### 2.6. Diffusion Bonding

For diffusion bonding, additional baffle plates, made of TZM, were used for protecting the pressure dies of the furnace from damaging. They were coated in a dense manner using alumina suspension to prevent sticking at the samples. 1) For diffusion bonding with zirconia beads, one sheet 0.2 mm in thickness with etches calottes and containing 50 µm zirconia beads was placed in between the two pieces of 40 mm round stock (see Figure 2).

2) For diffusion bonding with alumina-coated 100 µm sheets, ten coated sheets were separated by one uncoated sheet each, giving a stacked high of 1.9 mm, consisting of 19 layers between two pieces of 40 mm round stock.

After placing the samples in the furnace by *Maytec*, it was evacuated to a vacuum threshold better than  $1 \times 10^{-4}$  mbar. Afterwards, the temperature was ramped up at a rate of  $10 \text{ K min}^{-1}$  to a bonding temperature of  $T = 1075 \text{ }^\circ\text{C}$ . A contact

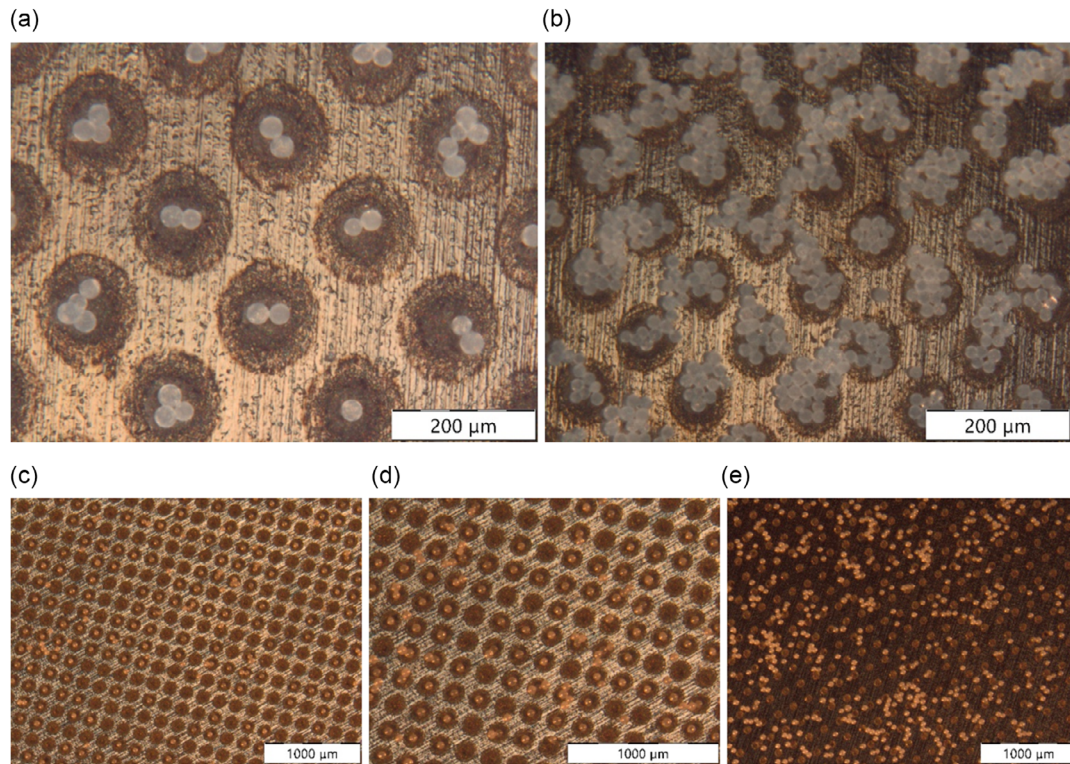


**Figure 9.** Assembly of zirconia beads within etched calottes. a,b) With 30  $\mu\text{m}$  zirconia beads. c–e) With 50  $\mu\text{m}$  zirconia beads.

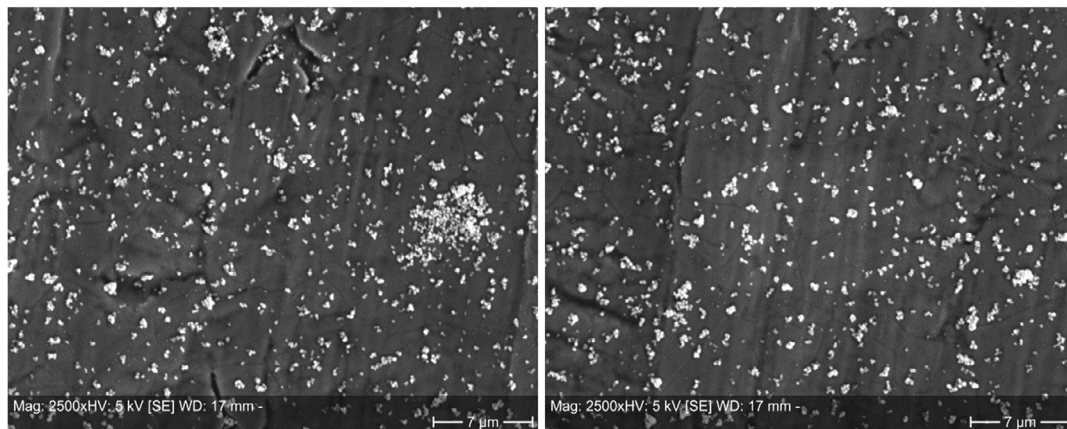


**Figure 10.** Alumina particles on dip-coated 100  $\mu\text{m}$  sheet material.

pressure of  $p = 16 \text{ MPa}$  was applied within 5 min and kept for a dwell time of  $t = 4 \text{ h}$ . After finishing diffusion bonding, the temperature was decreased at a rate of  $10 \text{ K min}^{-1}$ , and the furnace vented to ambient atmosphere pressure below  $190 \text{ }^\circ\text{C}$ .

For diffusion-bonded samples, metallographic views of the cross section are displayed in **Figure 11**. In a), the micrograph with 0.2 mm layer and 50  $\mu\text{m}$  zirconia beads is displayed. Obviously, the grain size of the round stock is much coarser than the thin sheet layer. There are no pores visible, and grain growth across the bonding plane occurred.

For the sample containing 19 100  $\mu\text{m}$  layers, ten of them coated with submicron alumina, grain growth across individual layers occurred. The layer thickness is  $\approx 90 \mu\text{m}$ . Some residual pores are visible.

### 3. Results

#### 3.1. Tensile Tests

It is known that thin sheet material made by cold rolling has a very fine grain microstructure due to multiple rolling and



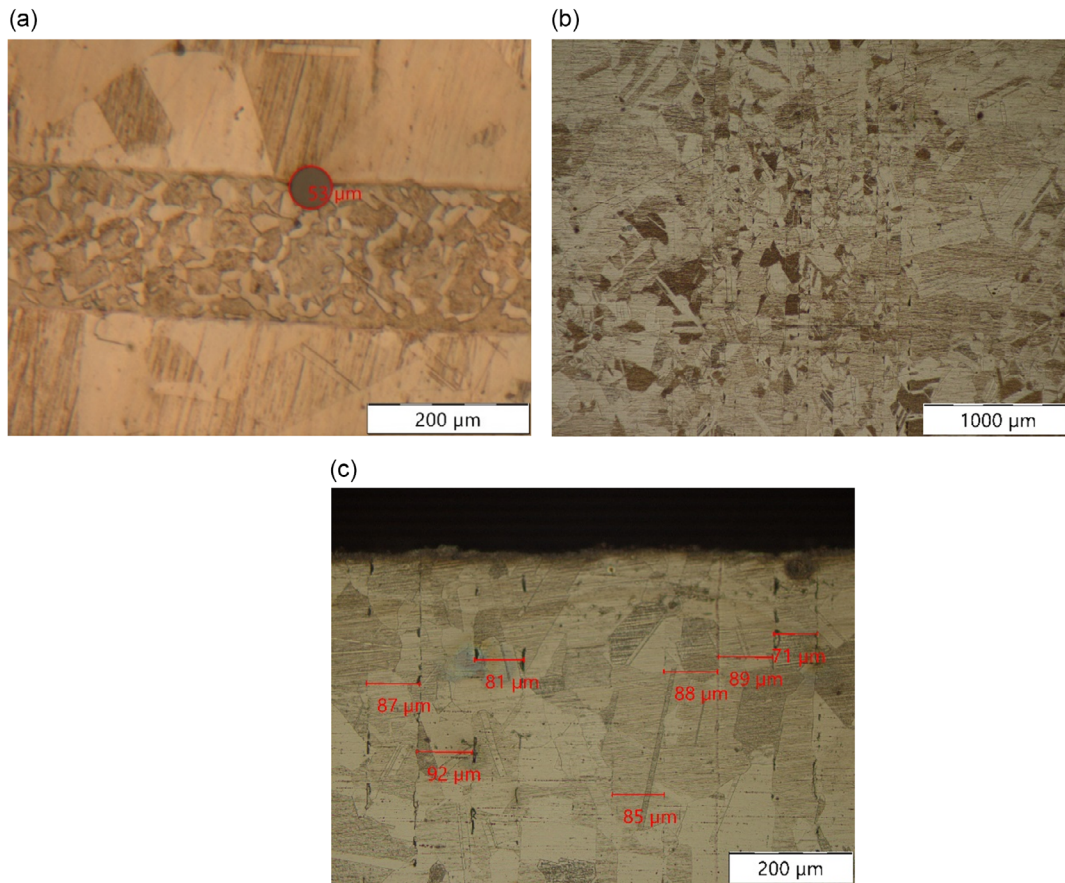


**Figure 11.** Cross sections of the diffusion-bonded samples. Bonding parameters:  $T = 1075\text{ }^{\circ}\text{C}$ ,  $t = 4\text{ h}$ ,  $p = 16\text{ MPa}$ . a) With a 0.2 mm-thick etched calotte sheet with  $50\text{ }\mu\text{m}$  zirconia beads. Note the zirconia bead in the bonding plane and different grain sizes of round stock and 0.2 mm layer. b,c) For the sample with 19 sheets,  $100\text{ }\mu\text{m}$  in nominal thickness. Ten of them were coated with submicron alumina and are separated by nine uncoated sheets. Note the grain growth across layers and remaining pores.

recrystallization heat treatments in between to limit forming forces. It leads to an increased strength due to *Hall–Petch* relation. In consequence, conventional tensile test bars would fail in the region of the 40 mm round stock with much larger grain size, regardless of any reinforcement effect due to ceramic particles and ODS effect in the bonding plane. Hence, a modified geometry of tensile test bar as displayed in **Figure 12b** was designed. It reduces the diameter from 5 to 3 mm, respectively, in the region of interest at the inserted layers reinforced with ceramic particles, ensuring failure within this area of interest.

However, from this modified geometry, it is not possible to give meaningful values for elongation at fracture, since only a very limited length of the samples is subjected to plastic deformation. In consequence, also the loading speed, related to the length participating in deformation, is much higher and does not meet the specification.<sup>[50]</sup> This has an impact on measured values for yield as well as tensile strength.<sup>[51]</sup> When analyzing the stress–strain curves, it has to be considered that the values were obtained from shorter test length (**Figure 13** and **14**).

For comparison reasons, standard tensile test samples of a constant diameter of 3 mm containing ten layers coated with submicron sized alumina, separated by nine uncoated layers, were performed for comparison reasons (**Figure 12a**).

However, it has to be mentioned that it is ambiguous to compare mechanical data of delivery and heat-treated state obtained from standard tensile test specimen to values from the modified tensile test geometry with locally reduced diameter: For face-centered cubic materials, usually, a yield strength  $R_{p0.2}$  for a remaining plastic deformation of 0.2% is specified, claiming that this low deformation does not affect functionality of a device. However, for the modified sample geometry, the deformation refers to a measuring length of 1 mm only at a higher load rate, instead of 15 mm for the standard geometry. Therefore, higher values for yield strength and tensile strength are expected for the modified sample geometry (**Table 2–3**).

From the  $d = 40\text{ mm}$  diffusion bonding samples, five tensile test specimens were wire eroded and machined in a way that the bonding plane was in the middle of the measuring length. Tensile tests were performed for all diffusion bonding experiments on at least five samples each. The tensile tests were

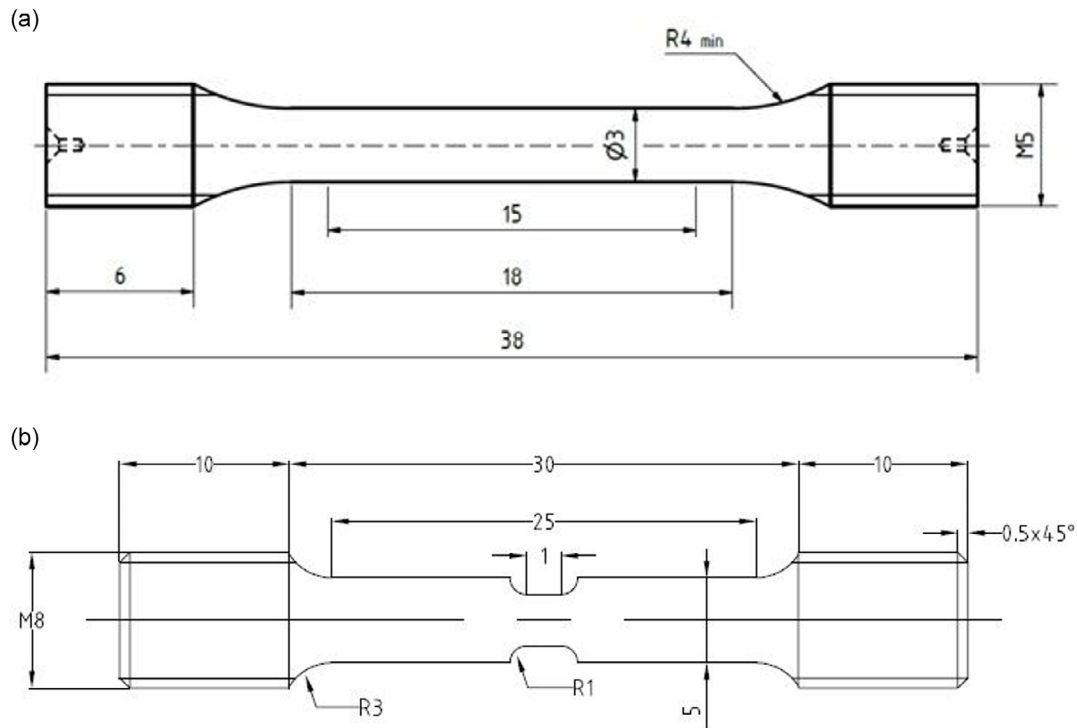


**Figure 12.** Dimensions of tensile test specimens. a) Regular tensile test bar,  $d = 3$  mm. b) Modified geometry with reduced thickness to 3 mm in the zone of interest.

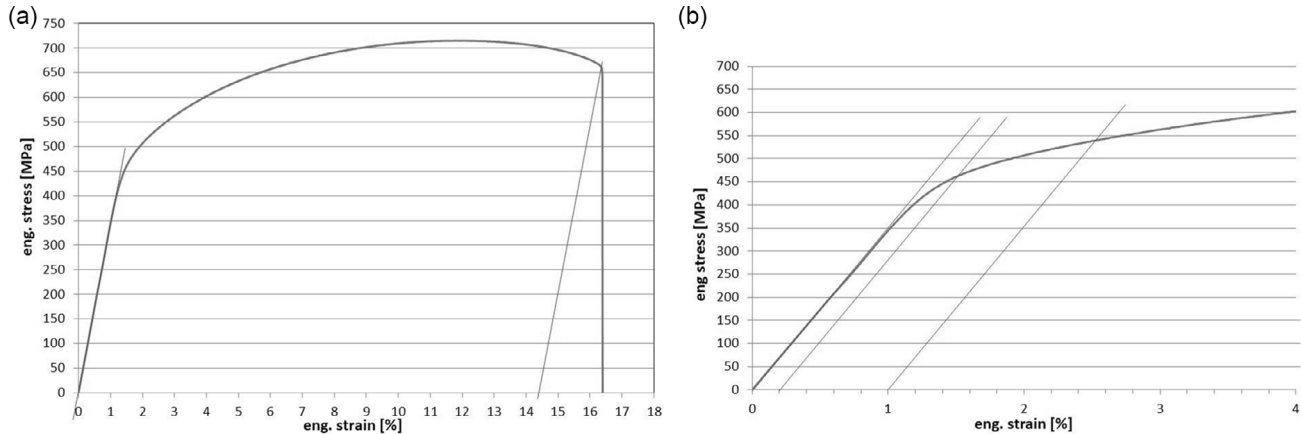


**Figure 13.** a) Stress–strain curve for sample no. 2. b) Detail for determination of  $R_{p0.2}$  and  $R_{p1.0}$ .

performed traverse controlled ( $dl/dt = 2 \text{ mm min}^{-1}$ ) using a universal testing machine from *Instron* (type 4505), equipped with a controller unit from *Doli*.

In the delivery condition, the mechanical data for the 40 mm round stock were 304.5 MPa for the yield strength ( $R_{p0.2}$ ), 652.7 MPa ( $R_m$ ) for tensile strength, giving a yield strength ratio of 0.47, and 79% for elongation at fracture ( $A_5$ ). After a heat treatment at  $T = 1100 \text{ }^\circ\text{C}$  and  $t = 4 \text{ h}$ , similar to diffusion bonding, values of 227 MPa, 588.5 MPa, and 95.9%, respectively, were obtained; see ref. [14]. The yield strength ratio was 0.39 after heat treatment. The thermal treatment causes a reduction of yield

strength by 25%. The tensile strength is reduced by 10%. The elongation at fracture, however, was increased by 20%. These effects can be attributed to recrystallization, accompanied by climbing and annihilation of dislocations and by grain growth. Any cold work hardening effect is lost during diffusion bonding.

In **Table 1–3**, the mechanical values for diffusion bonding experiments are given.

For some other nonferrous alloys, also values for  $R_{p1.0}$ , namely a plastic deformation of 1%, are given. For comparison reasons,  $R_{p1.0}$  values are given additionally from the slope of the stress–strain curve to assess the mode of failure.

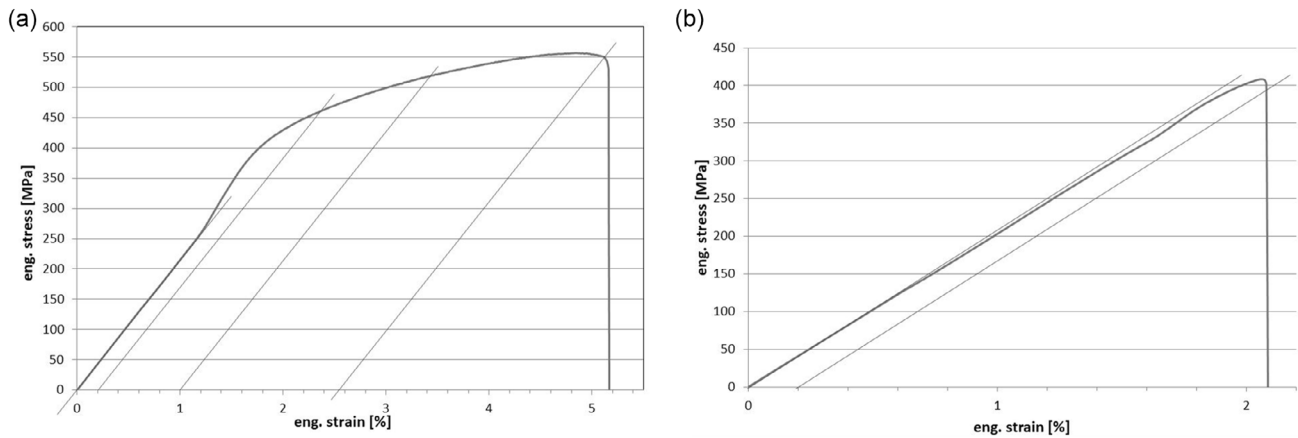


**Figure 14.** Stress–strain curve for a) sample no. 8 and b) sample no. 9, without plastic range, neglected in Table 2.

**Table 1.** Mechanical strength values of diffusion-bonded sample with microsieve and 50  $\mu\text{m}$  zirconia beads for modifies sample geometry.

Sample no.	$R_{p0.2}$ [MPa]	$R_{p1.0}$ [MPa]	$R_m$ [MPa]
1	486	553	724
2	467	542	716
3	482	550	723
4	453	533	712
5	475	545	718
<b>Average</b>	<b>472.6</b>	<b>544.6</b>	<b>718.6</b>
<b>StabwS</b>	<b>13.1</b>	<b>7.8</b>	<b>5.0</b>

**Table 2.** Mechanical strength values obtained for ten layers coated with submicron alumina, separated by nine uncoated layers for modified sample geometry.

Sample no.	$R_{p0.2}$ [MPa]	$R_{p1}$ [MPa]	$R_m$ [MPa]
6	433	505	545,4
7	430	484	488
8	459	518	557
10	450	514	565
<b>Average</b>	<b>443</b>	<b>505,25</b>	<b>538,9</b>
<b>StabwS</b>	<b>13,8</b>	<b>15,2</b>	<b>34,8</b>

### 3.1.1. Tensile Tests on Modified 3 mm Samples for Microsieve with 50 $\mu\text{m}$ Zirconia Beads and Alumina-Coated Interlayers

In Table 1, due to the modified sample geometry and shorter measuring length, the probability of a crack-inducing defect is lower than for the standard sample geometry. As the thickness of the inserted calotte plate is 0.2 mm only, it is fully within the length under investigation. Supported by the higher load speed, yield strength and tensile strength are higher than in the delivery state.

The yield strength ratio is 0.66 related to  $R_{p0.2}$  and 0.76 for  $R_{p1.0}$ , respectively. The scattering of mechanical values within the five samples is reasonably low.

**Table 3.** Mechanical strength values obtained for 3 mm standard tensile test samples for ten coated layers, separated by nine uncoated layers for standard geometry.

Sample no.	$R_{p0.2}$ [MPa]	$R_{p1.0}$ [MPa]	$R_m$ [MPa]	$\epsilon$ [%]	Remark
1	274	319	498	22,5	
2	278	319	528	27,5	
3	266	315	510	26	
4	263	310	511	27,8	
5	282	343	408	8,5	Delamination
6	266	315	315	1,4	Delamination
<b>Average</b>	<b>271.5</b>	<b>320.2</b>	<b>461.7</b>	<b>19.0</b>	
<b>StabwS</b>	<b>7.6</b>	<b>11.7</b>	<b>83.5</b>	<b>11.2</b>	

Taking a closer look at stress–strain curves (Figure 13), an elongation of about 15% can be recognized. This is much less than in delivery or heat-treated condition, despite the low length under consideration should contain less necking-inducing imperfections, and higher values of elongation should be expected. On the other hand, owing to the low measuring length, measuring inaccuracies is of increasing impact. Hence, in consequence, the inserted layer with 50  $\mu\text{m}$  zirconia beads must be considered as the reason for failure.

In Table 2, for the diffusion-bonded sample containing ten layers coated with submicron alumina, separated by nine uncoated layers, the width of inserted layers exceeds the measuring length of the modified sample geometry. From Figure 14, it can be seen that sample 9 failed without achieving a reasonable strength. SEM pictures showed large agglomerates of alumina at the fracture surface, preventing proper bonding. Hence, sample 9 was neglected for summarizing mechanical strength values in Table 2.

It is evident that none of the samples achieved any significant elongation at fracture. Obviously, due to the number of interfaces, there was always one weak bonding interface, which failed at low stress. This is supported by the results of the fracture surfaces in Section 3.2.



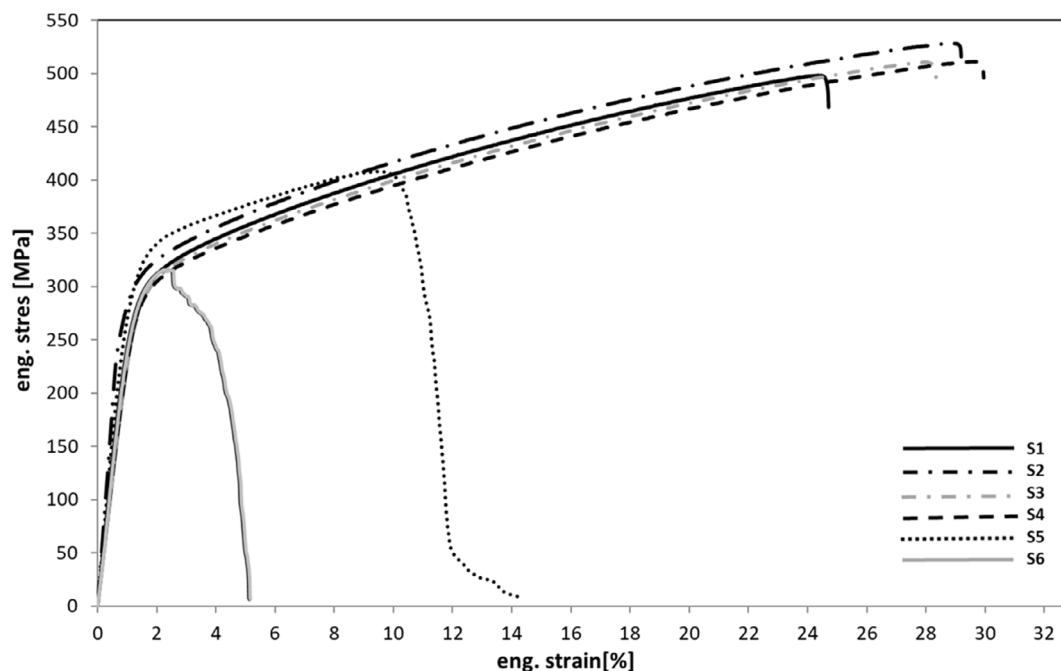


Figure 15. Results of tensile tests on 3 mm standard tensile test samples with ten alumina-coated layers, separated by nine uncoated layers.

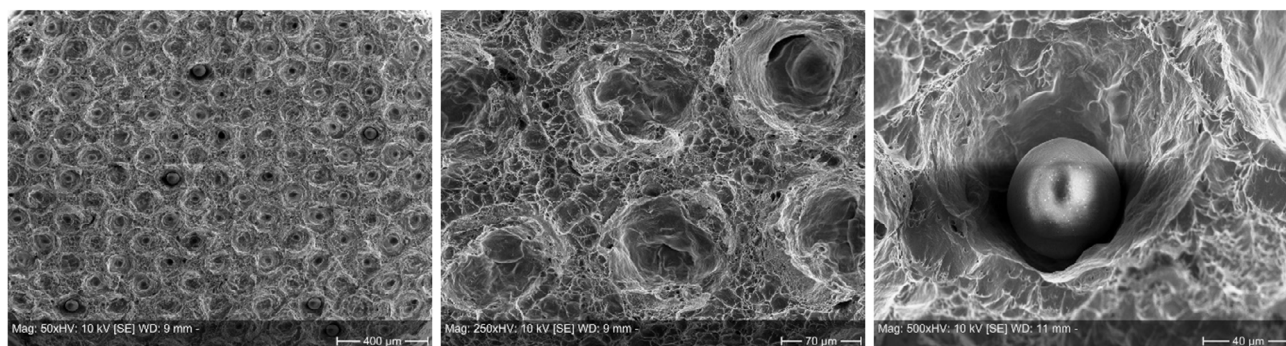


Figure 16. Magnification series of the fracture surface of modified 3 mm tensile test sample (Figure 12b), sample no. 1 (0.2 mm-thick sheet with etched calottes) with 50  $\mu\text{m}$  zirconia beads. Bonding parameters:  $T = 1075^\circ\text{C}$ ,  $t = 4\text{ h}$ ,  $p = 16\text{ MPa}$ .

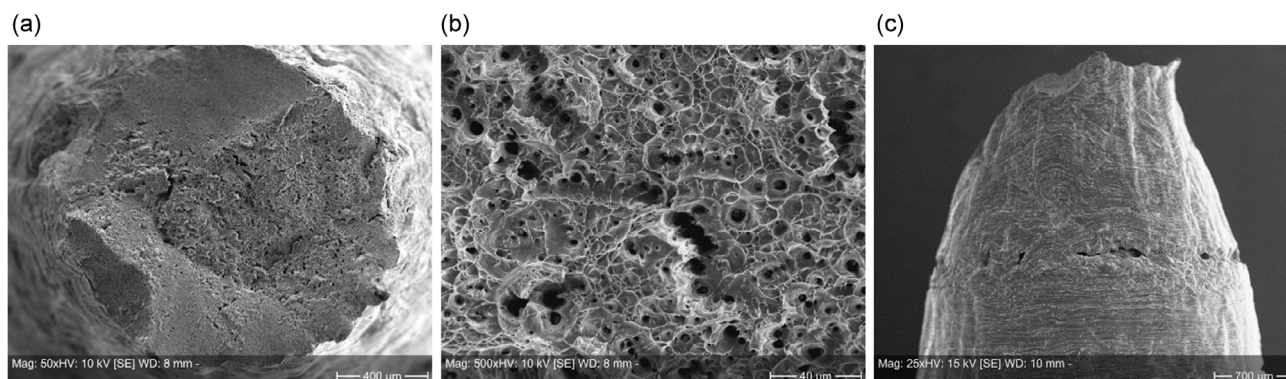


Figure 17. Fracture surface of modified 3 mm tensile test sample (Figure 12b), sample no. 4 (0.2 mm-thick sheet with etched calottes) with 50  $\mu\text{m}$  zirconia beads. a,b) Failure outside the layer with 50  $\mu\text{m}$  zirconia beads. c) Perimeter of sample 4. The layer of the 0.2 mm sheet can be recognized.



### 3.1.2. Tensile Tests Using 3 mm Standard Tensile Test Samples for Ten Alumina-Coated Layers, Separated by Nine Uncoated Layers

Compared Table 3 to the results displayed in Table 2 and Figure 14, the values obtained for the standard tensile test geometry and 19 layers are much lower, especially in respect to yield strength  $R_{p0.2}$  and  $R_{p1.0}$ , respectively (Table 3). The tensile strength, however, achieves only little lower values around 500 MPa, with exception of samples, showing delamination in different layers (compare Table 3, samples no. 5 and 6 to sample no. 9 in Table 2), leading to low elongation at fracture.

The loading speed for the standard geometry is one fifteenth compared to the modified sample geometry. In contrast to the modified sample geometry, the whole height of the stack consisting of 19 layers is within the measuring length. The probability of a local defect is therefore higher. As will be shown in Section 3.2, there are some agglomerations of alumina particles, which lead to high proportion of ceramic-metal interface that cannot transfer load and initiate failure. However, the elongation at fracture values is reasonable but much lower than in delivery or heat-treated condition. Sample nos. 5 and 6 show low elongations at fracture due

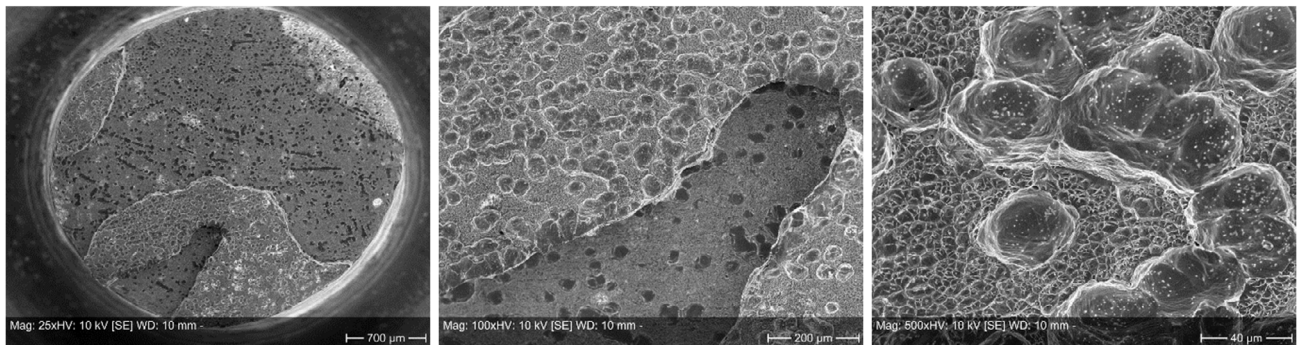


**Figure 18.** Magnification series of the fracture surface of modified 3 mm tensile test samples (see Figure 12b), sample no. 7 with 19 layers of 100  $\mu\text{m}$  sheets, ten of them coated with submicron alumina and separated by uncoated layers.

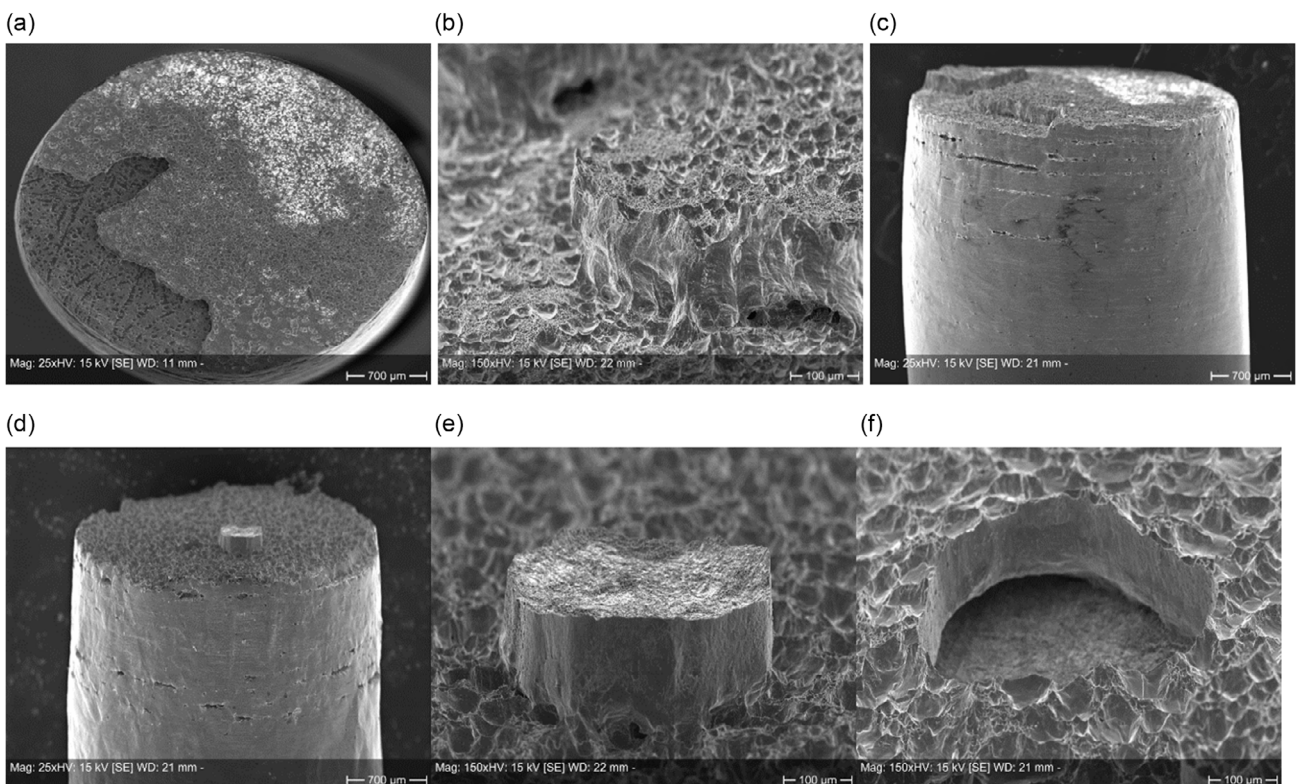


**Figure 19.** Magnification series of the fracture surfaces of 3 mm standard tensile test samples (Figure 12a) with 19 layers of 100  $\mu\text{m}$  sheets, ten of them coated with submicron alumina and separated by uncoated layers. a–c) Sample no. 6: irregular failure due to local agglomeration of alumina particles. d–f) Sample no. 4: mostly homogeneous and deformation-rich fracture with dimples and island-shaped layer residue. e) Alumina accumulation on torn out island. f) Counterpart of (e).

to delamination. All stress–strain curves are displayed in **Figure 15** for comparison reasons.

### 3.2. Evaluation of Fracture Surfaces

#### 3.2.1. For Samples with 0.2 mm Calotte Sheets and 50 $\mu\text{m}$ Zirconia Beads

Nearly all samples failed in the region of the ceramic-particle-reinforced layer. If all calottes would have been occupied by zirconia beads 50  $\mu\text{m}$  in diameter for a center-to-center distance of 255  $\mu\text{m}$ , about 6.1% of the total cross section would be ceramic–metal interface, not able to transfer any load. From **Figure 16**, it can be concluded that zirconia beads 50  $\mu\text{m}$  in diameter are too big to cause a reasonable reinforcing effect. Only sample no. 4 failed outside the plane of the inserted calotte sheet (**Figure 17**).

For other samples, the fracture surface shows a ductile failure with dimples between the wells where the zirconia beads were placed. Since it could not be guaranteed that each calotte had been filled, it is not possible to distinguish between originally filled and empty sites. Occasionally, some remaining zircons beads were found. However, it should be noted that unfilled areas are still recognizable as calottes. The diffusion bonding parameters were not sufficient to close these large defects through deformation and/or volume diffusion.

#### 3.2.2. For Samples with Nineteen 100 $\mu\text{m}$ Layers, Ten of Them Coated with Submicron Alumina

A different fracture mode was found for the samples containing 19 100  $\mu\text{m}$  layers, ten of them coated with submicron aluminum particles: here, the bonding of the layers was locally different, so material separation occurred at different spots of different bonded layers. As a result, the fracture surfaces of all samples show stain-like adhesions of different layers (**Figure 18**). Locally, areas with high plastic deformation and small dimples are visible. In all dimples, particles of alumina were found and confirmed by energy-dispersive X-ray spectroscopy (EDX) measurements. However, due to the submicron size of the alumina, stainless steel was always included in the measurement and hence, EDX measurements are not displayed here in detail.

In **Figure 19**, at the perimeter of the 3 mm tensile test sample, crack initiation at different layers can be detected. On the one hand, the layer-by-layer failure must be considered as the reason for the significantly reduced elongation at fracture. On the other hand, it can be seen from the sample surface that areas outside the 19 layers contributed to deformation, too. A certain reinforcing effect can be stated; however, the elongation at fracture is far away from samples without ceramic particles.

## 4. Conclusion and Outlook

In this article, two different approaches of taking advantage of reinforcing by means of the ODS effect inside a diffusion bonding layer are presented.

It is concluded that zirconia beads several tens of micrometers in size are not suitable to obtain a reinforcing effect. The percentage of ceramic–metal interface at the total cross section exceeds

the reinforcing effect by far. Furthermore, no satisfactory method to distribute the zirconia beads homogeneously inside calottes or holes was found. Obviously, attractive forces prevent separation to individual beads. Preventing beads to go under the etched sheets (in case of double side etched holes) or forcing beads over the surface to occupy all designated places (in case of single side etched calottes) could not be achieved by simple means.

More promising was the application of submicron sized alumina by dip coating of sheet material in diluted dispersion: Over a wide range of sheet material, isolated ceramic particles were found, leading to a pronounced dimple-rich ductile fracture surface. However, some areas with agglomerates were detected, initiating an early stage of fracture.

In general, for both approaches, problems arose for the application and equal distribution of the ceramic particles. For the zirconia beads, adhesion prevented equal filling of all recesses. In case of submicron alumina, local accumulation of agglomerates could not be eliminated so far. However, it seems that submicron alumina particles had a reinforcing effect, since fracture surfaces showed a ductile failure, rich in dimples. In all dimples, isolated particles of alumina were found. Further attempts should be made to improve the homogeneous distribution of submicron alumina and prevent local accumulation of agglomerates.

Using a modified specimen geometry for tensile tests makes it more difficult to compare the results obtained. The separation of the effects of the higher strength of thin sheet metal layers, possessing a small grain size on one hand, and the reinforcing effect of small ceramic particles as well as its impact on a reduction of mechanical properties due to ceramic–metal interface, remains challenging and is worth investigating.

## Acknowledgements

The financial support from the Helmholtz Program SCI (Storage and Cross-linked Infrastructure) is gratefully acknowledged.

Open Access funding enabled and organized by Projekt DEAL.

## Conflict of Interest

The authors declare no conflict of interest.

## Data Availability Statement

The data that support the findings of this study are available from the corresponding author upon reasonable request.

## Keywords

ceramic nanoparticles, diffusion bonding, diffusion welding, oxide dispersion strengthening effect, reinforcing

Received: March 3, 2025

Revised: July 7, 2025

Published online:



- [1] M. W. Mahoney, C. C. Bampton, in *Welding, Brazing and Soldering*, ASM Handbook, Vol. 6 (Eds: D. L. Olson, T. A. Siewert, S. L. Liu, G. R. Edwards), ASM International, Almere, Netherlands **1993**.
- [2] H. P. Mahajan, L. M. A. Lima, T. Hassan, *J. Mater. Technol.* **2022**, 144, <https://doi.org/10.1115/1.4052825>.
- [3] W. Sittel, W. Basuki, J. Aktaa, *J. Nucl. Mater.* **2015**, 465, <https://doi.org/10.1016/j.jnucmat.2015.05.056>.
- [4] C. Zhang, H. Li, M. Li, *JOM* **2019**, 3, <https://doi.org/10.1007/s11837-018-3300-7>.
- [5] S. H. Kim, J.-H. Cha, C. Jang, I. San, *Metals* **2020**, 10, <https://doi.org/10.3390/met10040480>.
- [6] V. R. Saranam, B. K. Paul, *Proc. Manuf.* **2018**, 26, <https://doi.org/10.1016/j.promfg.2018.07.066>.
- [7] S. Li, P. Liu, Y. Chen, Y. Peng, W. Guo, J. Xiong, J. Li, *Mater. Charact.* **2023**, 203, <https://doi.org/10.1016/j.matchar.2023.113161>.
- [8] H. Zhang, J. Li, P. Ma, J. Xiong, F. Zhang, *Vacuum* **2018**, 152, <https://doi.org/10.1016/j.vacuum.2018.03.019>.
- [9] G. Sharma, D. K. Dwivedi, *Int. J. Adv. Manuf. Technol.* **2018**, 95, <https://doi.org/10.1007/s00170-017-1490-8>.
- [10] G. Thirunavukarasu, S. Kundu, *JMEPEG* **2019**, 29, <https://doi.org/10.1007/s11665-019-04498-x>.
- [11] W. Gao, S. Xing, J. Lei, *SN Appl. Sci.* **2020**, 2, <https://doi.org/10.1007/s42452-020-03760-5>.
- [12] in *Materialwissenschaft und Werkstofftechnik*, 4th ed. (Ed: G. Gottstein), Springer Vieweg, Berlin, Heidelberg **2014**, p. 198.
- [13] Y. Peng, Z. X. Li, W. Guo, J. T. Xiong, J. L. Li, *J. Mater. Process. Technol.* **2024**, 324, <https://doi.org/10.1016/j.jmatprotec.2023.118267>.
- [14] T. Gietzelt, M. Walter, V. Toth, F. Messerschmidt, M. Blem, *Adv. Eng. Mater.* **2021**, 23, <https://doi.org/10.1002/adem.202100188>.
- [15] T. Gietzelt, V. Toth, A. Huell, R. Dittmeyer, *Adv. Eng. Mater.* **2017**, 19, <https://doi.org/10.1002/adem.201600344>.
- [16] L. Yuan, J. Xiong, Y. Peng, J. Shi, J. Li, *MSEA* **2020**, 772, <https://doi.org/10.1016/j.msea.2019.138670>.
- [17] S. Sam, S. Kundu, C. Chatterjee, *Mater. Des.* **2012**, 40, <https://doi.org/10.1016/j.matdes.2012.02.058>.
- [18] G. Thirunavukarasu, S. Kundu, *JMEP* **2020**, 29, <https://doi.org/10.1007/s11665-019-04498-x>.
- [19] in *Recrystallization and Related Annealing Phenomena*, 1st ed., 2nd Impression (Eds: F. J. Humphreys, M. Hatherly), Elsevier Science Ltd., Oxford, UK **2002**, p. 281ff.
- [20] in *Sintering of Advanced Materials, Fundamentals and Processes*, 1st ed., (Ed: Z. Z. Fang), Woodhead Publishing, Oxford, UK **2010**, p. 36ff.
- [21] P. R. Rios, F. Siciliano, H. R. Z. Sandim, R. L. Plaut, A. F. Padilha, *Mater. Res.* **2005**, 8, <https://doi.org/10.1590/S1516-14392005000300002>.
- [22] D. Hull, D. J. Bacon, *Introduction To Dislocations, Chapter 9*, 5th ed, Elsevier, Amsterdam **2011**, <https://doi.org/10.1016/C2009-0-64358-0>.
- [23] G. Z. Voyiadjis, M. Yaghoobi, *Size Effects in Plasticity: From Macro to Nano*, Elsevier Academic Press, London **2020**, <https://doi.org/10.1016/B978-0-12-812236-5.00001-3>.
- [24] T. Gietzelt, V. Toth, A. Huell, *Adv. Eng. Mater.* **2018**, 20, <https://doi.org/10.1002/adem.201700367>.
- [25] CEP Freiberg, High temperature materials, see under download "Broschüre Kupfer-Hochtemperaturwerkstoffe", p. 5, [www.cep-freiberg.de/de/download](http://www.cep-freiberg.de/de/download), (accessed: 03 July 2025).
- [26] D. Mao, Y. Xie, X. Meng, X. Ma, Z. Zhang, X. Sun, L. Wan, K. Volodymyr, Y. Huang, *Mater. Horiz.* **2024**, 11, <https://doi.org/10.1039/D4MH00139G>.
- [27] K. O. Cooke, A. Richardson, T. I. Khan, M. A. Shar, *J. Manuf. Mater. Process* **2020**, 4, <https://doi.org/10.3390/jmmp4010003>.
- [28] G. Gottstein, *Physikalische Grundlagen der Materialkunde*, 3rd ed., Springer, Berlin, Heidelberg, New York **2007**, p. 165ff.
- [29] Properties for cold rolled sheet material, see under [www.montanstahl.com/de/magazin/kaltwalz-technologie-kaltwalzen-edelstahl/](http://www.montanstahl.com/de/magazin/kaltwalz-technologie-kaltwalzen-edelstahl/) (accessed: 03 July 2025).
- [30] Tolerances of thin sheet material, see DIN EN 10131 **2006**, Beuth Verlag, Berlin
- [31] in *Functional Materials: Preparation, Processing and Applications* (Eds: S. Banerjee, A. K. Tyagi), Elsevier, London, Waltham **2012**, pp. 475 ff, Ch. 11.
- [32] Hot and cold rolling: Advantages and disadvantages, see under [de.materials4me.com/wissen-ideen/allgemeine-werkstoff-themen/produktionsmethoden-von-metallprofilen](http://de.materials4me.com/wissen-ideen/allgemeine-werkstoff-themen/produktionsmethoden-von-metallprofilen), (accessed: 03 July 2025).
- [33] T. Gietzelt, V. Toth, H. Lambach, R. Dittmeyer, *Adv. Eng. Mater.* **2013**, 15, <https://doi.org/10.1002/adem.201200339>.
- [34] T. Harumoto, Y. Yamashita, O. Ohsahi, T. Ishiguro, *Mater. Trans.* **2014**, 55, <https://doi.org/10.2320/matertrans.M2013405>.
- [35] B. Xie, M. Sun, B. Xu, C. Wang, H. Jiang, D. Li, Y. Li, *Corr. Sci.* **2019**, 147, <https://doi.org/10.1016/j.corsci.2018.11.001>.
- [36] T. Gietzelt, V. Toth, T. Weingärtner, *Mat.-wiss. u. Werkstofftech.* **2018**, 9, <https://doi.org/10.1002/mawe.201800197>.
- [37] Y. Guo, Y. Wang, B. Gao, Z. Shi, Z. Yuan, *Ceram. Int.* **2016**, 42, <https://doi.org/10.1016/j.ceramint.2016.07.145>.
- [38] C. Zhang, H. Li, M. Q. Li, *Vacuum* **2017**, 137, <https://doi.org/10.1016/j.vacuum.2016.12.021>.
- [39] Z. Guoge, R. S. Chandel, *J. Mater. Sci.* **2005**, 40, <https://doi.org/10.1007/s10853-005-0696-6>.
- [40] C. Zhang, H. Li, M. Q. Li, *Appl. Surf. Sci.* **2016**, 371, <https://doi.org/10.1016/j.apsusc.2016.03.039>.
- [41] I. Jauhari, H. Ogiyama, H. Tsukuda, *Mater. Sci. Res. Int.* **2003**, 9, 154.
- [42] G. Luo, J. He, Z. Song, M. Rao, J. Mo, Y. Wang, Q. Shen, L. Zhang, *J. Mater. Eng. Perform.* **2019**, 28, <https://doi.org/10.1007/s11665-019-3856-6>.
- [43] G. Chen, Z. Feng, J. Chen, L. Liu, H. Li, Q. Liu, S. Zhang, X. Cao, G. Zhang, Q. Shi, *Scr. Mater.* **2017**, 128, <https://doi.org/10.1016/j.scriptamat.2016.10.015>.
- [44] F. R. Morral, "Dispersion Strengthening of Metals", Metals and Ceramics Information Center, MCIC77-30 Report, Metals and Ceramics Information Center, **1977**, see under [https://books.google.de/books?id=WZhtAAAAAAJ&pg=PR1&hl=de&source=gbs\\_selected\\_pages&cad=1#v=onepage&q&f=false](https://books.google.de/books?id=WZhtAAAAAAJ&pg=PR1&hl=de&source=gbs_selected_pages&cad=1#v=onepage&q&f=false), (accessed: 03 July 2025).
- [45] E. Simondon, P.-F. Giroux, J. Ribis, G. Spartacus, L. Chaffron, T. Gloriant, *Mat. Char.* **2021**, 181, <https://doi.org/10.1016/j.matchar.2021.111461>.
- [46] K. O. Cooke, *Metall. Mater. Trans. B* **2012**, 43, <https://doi.org/10.1007/s11663-012-9643-5>.
- [47] Product specifications of zirconia beads by Tosoh, see under [www.tosoh-europe.com/our-products/grinding-media](http://www.tosoh-europe.com/our-products/grinding-media), (accessed: 03 July 2025).
- [48] Product specifications for sodium carboxymethyl cellulose polymer TEXTURECEL 2000 PA 07, see under [www.industrialcellulosics.com/products/texturecel/texturecel-crt-2000-pa-07](http://www.industrialcellulosics.com/products/texturecel/texturecel-crt-2000-pa-07), (accessed: 03 July 2025).
- [49] Product specifications for alumina Baikowski CR6, see under <https://www.baikowski.com/en/serie/cr/>, (accessed: 03 July 2025).
- [50] Tensile Test, DIN EN ISO 6892-1: Metallische Werkstoffe – Zugversuch – Teil 1: Prüfverfahren bei Raumtemperatur (ISO 6892-1:2016), DIN Deutsches Institut für Normung e. V., DIN-Normenausschuss Materialprüfung (NMP).
- [51] S. Kalpakjian, S. R. Schmid, E. Werner, *Werkstofftechnik – Herstellung, Verarbeitung, Fertigung*, 5th ed., Pearson Benelux B.V., München **2011**, p. 89ff.